J Electroceram (2011) 26:14–22
DOI 10.1007/s10832-010-9621-8

MEMS interdigitated electrode pattern optimization for a unimorph piezoelectric beam

Ryan R. Knight · Changki Mo · William W. Clark

Received: 20 October 2009 / Accepted: 4 October 2010 / Published online: 21 October 2010

Abstract This paper presents optimization of interdigitated (d_{33}) piezoelectric MEMS unimorph cantilever beams for harvesting vibration energy or for tuning resonators. The analysis of the poling behavior of the piezoelectric material is the key feature. While it is common that simplified models of interdigitated piezoelectric devices assume some uniform and well-defined poling pattern, the finite element modeling used in this work shows that not to be the case. A percent poling factor is developed to investigate the real losses associated with non-uniform poling. A parametric study in terms of electrode patterns, piezoelectric layer dimensions, and electrode dimensions is carried out to examine their effect on the percent poling factor. Design guidelines are provided to help ensure that such piezoelectric MEMS devices are developed to obtain optimum energy harvesting or tuning performance.

Keywords MEMS · Piezoelectric · Interdigitated · Electrode · Energy harvesting · Finite element analysis

1 Introduction

Piezoelectric materials are incorporated into many of today's commercial and research applications. Accelerometers, crystal oscillators, sonar, audio transducers, igniters, positioning systems, vibrations absorbers, and energy harvesters are a few examples. The development of thin film PZT (lead zirconate titanate) fabrication and all of the research dedicated to it has spawned many applications in MEMS. Of those, two devices of particular interest in this work are MEMS piezoelectric harvesters and tunable piezoelectric resonators.

MEMS piezoelectric harvesters have been investigated, built, and tested by a number of researchers, including Sood et al. [1], Jeon et al. [2], Choi et al. [3], Shen et al. [4], Lee et al. [5], Reilly and Wright [6], and so on. In particular, the group of researchers [1–3] was the first to develop MEMS scale energy harvesting structures and present empirical power data for MEMS scale structures. Their MEMS energy harvester could generate about 1 μW of power. In each of these works, interdigitated electrode (IDE) d_{33} mode MEMS cantilevers were developed and tested because the high output voltage of the mode would be able to overcome the forward bias from the rectifying circuit. While PZT was used in that research, other efforts by Hong et al. [7] and John et al. [8] looked at using a PMN-PT (Lead magnesium niobate- lead titanate) as the piezoelectric material for the MEMS harvesting structure.

MEMS piezoelectric resonators have been developed and tested by DeVoe [9], Li et al. [10], Piazza et al. [11], Dai et al. [12], Mestrom et al. [13], Lopez et al. [14], and so many others. Recently, a variety of research on frequency tunable MEMS resonators and filters has also been conducted [15–24]. Among those studies, efforts by Frederick [23] and Knight [24] have focused on tuning the frequency of the piezoelectric MEMS device by adjusting the electrical boundary conditions on a portion of the piezoelectric material in the structure. This tuning concept was based on previous studies by Clark [25], Davis

R. R. Knight · W. W. Clark
Mechanical Engineering and Materials Science Department,
University of Pittsburgh,
Pittsburgh, PA 15260, USA

C. Mo (✉)
School of Mechanical and Materials Engineering,
Washington State University-Tri-Cities,
2710 Crimson Way,
Richland, WA 99354, USA
e-mail: changki.mo@tricity.wsu.edu

et al. [26], Lesientre et al. [27], Muriuki [28], and Wu et al. [29], even though much of this work was done on theoretical or macro scale resonator structures.

In both the harvester and the resonator devices, the question of optimal electrode patterns and dimensions is an open issue when the devices are built at the MEMS scale and utilize IDE.

At the micro-scale, it is easier to fabricate interdigitated piezoelectric beams than conventional (d_{31}) beams because of the reduced number of layers required. Given the small dimensions, however, it can be difficult to achieve electrode patterns that have ratios of spacing and width-to-thickness that are commonly found in macro-scale interdigitated beams. This paper considers the effects of electrode patterns and dimensions on the real piezoelectric material poling.

The interdigitated beam utilizes the d_{33} piezoelectric constant. The d_{33} constant for PZT is commonly known to be approximately twice as large as the d_{31} constant. Therefore, designing a d_{33} structure properly could produce more energy and larger tuning range than a d_{31} structure. However, depending on the electrode spacing and the piezoelectric layer thickness this assumption might not be valid. In this regard the poling electric field is examined in this study [24]. Following the simulation of the beam's poling electric field, the non-uniform electric field loss is then presented. A model is produced that simulates various IDE geometries and calculates the electric field density in the piezoelectric layer. An optimal ratio of electrode width to piezoelectric layer thickness is also found from the finite element analysis (FEA) simulations, and the planar IDE loss or percent poling is analyzed.

2 Mathematical piezoelectric beam models

2.1 Unimorph d_{31} beam model

A uniform d_{31} beam is a cantilever beam composed of two main layers. These two main layers are the substrate layer and the piezoelectric layer. Figure 1 shows a typical d_{31} beam.

The gold layer in Fig. 1 is the electrode deposited on top of the piezoelectric layer. This layer is typically thin

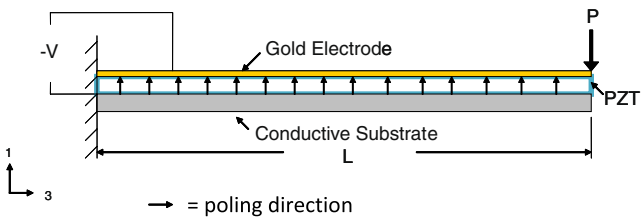

Fig. 1 Unimorph d_{31} beam

(~3000 Å) and is commonly neglected in mechanical models. The electrode layer is used to pole the piezoelectric material in the thickness direction. Additionally, the electrode layer is used for charge collection in an energy harvester.

The energy of a unimorph d_{31} beam is derived from the combination of the piezoelectric and structural layers. Kim [30] shows that the energy produced from a cantilever beam under a static end load is

$$U_{Gen} = \frac{1}{2}\frac{Q_{Gen}^2}{C_{oc}} \tag{1}$$

The generated charge Q_{Gen} and the open circuit capacitance C_{oc} in the d_{31} beam can be found as

$$Q_{31Gen} = -\frac{3d_{31}s_{11}s_{11}^E h_m\left(h_m + h_p\right)L^2}{B_{11}}P \tag{2}$$

$$C_{31oc} = \frac{\varepsilon_{33}^T WL}{h_p}\left[1 + \left(\frac{3s_{11}^{E\,2}s_{11}h_p h_m^2\left(h_m + h_p\right)^2}{(s_{11}^E h_m + s_{11}h_p)B_{11}} - 1\right)K_{31}{}^2\right] \tag{3}$$

where s_{11} is the substrate elastic compliance, s_{11}^E is the PZT elastic compliance in the d_{31} mode, h_m is the substrate thickness, h_p is the PZT thickness, L is the beam length, W is the beam width, ε_{33}^T is the permittivity of the piezoelectric material at constant stress, and two other constants in Eq. 3 are defined as

$$B_{11} = \left(s_{11}h_p^2\right)^2 + 4s_{11}^E s_{11}h_m h_p^3 + 6s_{11}^E s_{11}h_m^2 h_p^2 + 4s_{11}^E s_{11}h_m^3 h_p + \left(s_{11}^E h_m\right)^2, \text{and } K_{31} = d_{31}\Big/\sqrt{\varepsilon_{33}^T s_{11}^E}$$

2.2 Interdigitated unimorph d_{33} beam model

Figure 2 depicts a common interdigitated d_{33} beam design. The piezoelectric material is poled along the length of the beam, towards the anode, and all the material underneath the electrode is assumed to be poled. Figure 3 illustrates this assumption.

The derivation of the energy equations for an IDE d_{33} beam follows the approach by Kim [30] and Mo et al. [31, 32]. The d_{31} beam model is integrated uniformly across the length while the d_{33} beam is broken up into individual

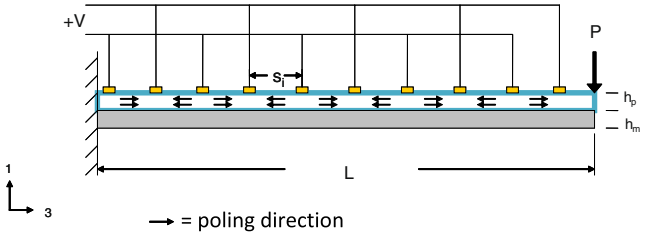

Fig. 2 Typical interdigitated unimorph d_{33} beam

sections between each electrode. The total generated electrical energy can be found as

$$U = \sum_{i=1}^{n} \int_{s_i} \int_{0}^{W} \left(\int_{0}^{h_p} dU_p dz + \int_{-h_m}^{0} dU_m dz \right) dy dx \qquad (4)$$

In Eq. 4, dU_p and dU_m are the energy terms for small volumes of the piezoelectric and substrate materials [31, 32]. The parameter s_i refers to each individual section between the electrodes. For each segment spacing, s_i, a percentage of the piezoelectric material is considered to be poled in the 3-direction, as defined by the percent poling factor, $\%d_{33}$, which can vary from 0 to 1. The schematic shown in Fig. 3 depicts a case where $\%d_{33}$=1, because all of the piezoelectric material is assumed to be poled in as d_{33}. In reality, as will be discussed later, this is not the case, and the resulting harvesting or tuning performance is less than ideal.

Considering the percent poling factor, the generated charge Q_{Gen} and open circuit capacitance C_{oc} in the d_{33} beam are

$$Q_{33Gen} = -\frac{3(\%d_{33}) s_{33} s_{33}^E h_m h_p (h_m + h_p)}{B_{33}} Pn \left(\sum_{i=1}^{n} (s_i) \right) \qquad (5)$$

$$C_{33oc} = \left[1 + \left(\frac{3 s_{33}^{E^2} s_{33} h_p h_m^2 (h_m + h_p)^2}{(s_{33}^E h_m + s_{33} h_p) B_{33}} - 1 \right) (K_{33})^2 \right] \sum_{i=1}^{n} C_i \qquad (6)$$

where s_{33} is the substrate elastic compliance, s_{33}^E is the PZT elastic compliance in the d_{33} mode, n is the number of sections, and other constants are defined as $B_{33} = \left(s_{33} h_p^2 \right)^2 + 4 s_{33}^E s_{33} h_m h_p^3 + 6 s_{33}^E s_{33} h_m^2 h_p^2 + 4 s_{33}^E s_{33} h_m^3 h_p + \left(s_{33}^E h_m \right)^2$, $K_{33} = \%d_{33} \Big/ \sqrt{\varepsilon_{33}^T s_{33}^E}$, and $C_i = \frac{\varepsilon_{33}^T W h_p}{s_i}$.

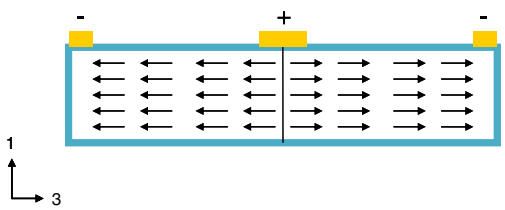

Fig. 3 Magnified view of the piezoelectric layer of IDE d_{33} beam

The percent poling factor, $\%d_{33}$, depends on the spacing and will be shown later to approach one as the spacing, s_i, increases. Therefore, different spacing values will correspond to different percent poling factors. Q_{gen} and C_{oc} are left in a summation form because the parameter s_i can be varied depending on the electrode spacing.

2.3 Comparing two modes of the unimorph

Sodano et al. [33, 34] compared these two types of harvesting designs for power generation. They experimentally found that the d_{31} unimorph as in Fig. 1 performed the best in comparison to the IDE designs. The underlying culprit for the poor harvesting characteristics of the d_{33} design is that area is sacrificed when using the IDE layout. This can simply be seen from the following energy equation

$$E_c = \frac{1}{2} C V^2 \qquad (7)$$

Equation 7 states that the energy of a capacitor is equivalent to half the capacitance multiplied by the corresponding voltage squared. The IDE layouts investigated significantly decrease the capacitance which limits the energy harvesting capabilities. However, a properly designed d_{33} beam has the capability to produce the same energy as a d_{31} beam and possibly even more. This is because the d_{33} constant is significantly greater than the d_{33} constant. In order to compare the performance of the d_{31} and d_{33} unimorphs, the parameters of the energy are investigated.

From Eq. 1 both of the d_{31} and d_{33} unimorphs' energy values are functions of Q_{gen} and C_{oc}. Taking the ratio of these parameters will create some insight into how these structures compare. The ratio of the d_{33} unimorph's capacitance to the d_{31} unimorph's capacitance is

$$\frac{C_{33oc}}{C_{31oc}} = \left(\gamma_1 \left(\frac{K_{33}}{K_{31}} \right)^2 \right) \frac{\sum_{i=1}^{n} \frac{\varepsilon_{33}^T W h_p}{s_i}}{\frac{\varepsilon_{33}^T W L}{h_p}} \qquad (8)$$

γ_1 is related to the ratio of $\frac{s_{33}^E}{s_{11}^E}$ and other structural parameters that do not change the ratio since those are equal for the two beams.

The ratio of the d_{33} unimorph's generated charge to the d_{31} unimorph's charge is then

$$\frac{Q_{33gen}}{Q_{31gen}} = \frac{\gamma_2 \left(\frac{\%d_{33}}{d_{31}} \right) n^2 \sum_{i=1}^{n} (s_i)}{L^3} \qquad (9)$$

where γ_2 is also related to the ratio of $\frac{s_{33}^E}{s_{11}^E}$ and other structural parameters.

Analyzing Eqs. (8) and (9), one can determine which design will be better for its application. If the ratios are greater than one then the d_{33} unimorph should be considered. If the ratios are less than one a d_{31} unimorph should be considered. Moreover, lower capacitance, *C,* implies that the structure is well-suited for tuning while higher generated charge, *Q,* implies that the structure is good for energy harvesting. Since $d_{33}>d_{31}$ for PZT the ratios naturally seem to lean towards a d_{33} unimorph. One would think that the d_{33} unimorph is the best design. But because of the percent loss factor, the generated charge Q_{33gen} is typically less than Q_{31gen} which implies that the d_{33} unimorph may not be as well suited for energy harvesting applications.

3 Interdigitated electrode analysis and optimization

The d_{33} IDE beam was modeled using ANSYS™ 10.0. In order to model the behavior associated with the piezoelectric layer a coupled field analysis was undertaken. Solid 95 elements were used to model the electrode and Solid 226 coupled field elements were used to model the piezoelectricity. The PZT layer was considered to be isotropic but was put into ANSYS as a 6x6 isotropic compliance matrix. The poling electric field was first examined. An optimal electrode width to piezoelectric thickness ratio is found from the FEA simulations. The planar IDE loss or percent poling was then analyzed.

3.1 Simulation of poling electric field and the percent loss factor

To better understand what direction the PZT is being poled in the IDE configuration a FEA model was built that simulates the electric field during poling. Figure 4 shows the top view of the IDE beam. The picture on the left in Fig. 4 is the actual ANSYS™ model [35]. The picture on the right of Fig. 4 shows the same picture as on the left except that the IDE electrodes are superimposed onto the model to making the IDE easier to distinguish.

The beam is surrounded by air to help accurately model the electric field. The area surrounding the rectangular beam in Fig. 4 is modeled as air. Two oppositely-poled electrodes on each side of the beam run down the length of the beam. These electrodes are connected to electrode fingers that run parallel to the width. Ideally the d_{33} mode is to be created between these fingers such that the beam is poled along its length, however the finite element model suggests that this may not actually occur, depending on the dimensions of electrodes and spacings.

As an example case, the poling voltage was set to 75 Volts on one electrode and 0 Volts on the other. The finite element results for the simulated electric field are shown in Fig. 5.

Figure 5 shows a close-up of the electric field vectors between two electrodes. The left picture in Fig. 5 highlights the area between the electrodes whereas the right picture is a zoom-in view of the electric field results. Since the electrodes are conductive they appear as darker rectangular regions in Fig. 5. This analysis was 3-D so some of the electric field vectors point into and out of the page. The corona effect is produced at the corners and edges of the electrode. This is because the magnitude of electric field is inversely proportional to radius of curvature. The poling electric field has two major directions: 1) the diagonal direction between each electrode and 2) in the width direction. Therefore conservatively, less than half (and probably much lower) of PZT was poled in the length or the assumed 3-direction in this example. The 3-direction is assumed to be in the length direction for an IDE d_{33} unimorph. A small amount of the PZT being poled in the length direction will provide poorer-than expected tuning or energy harvesting performance.

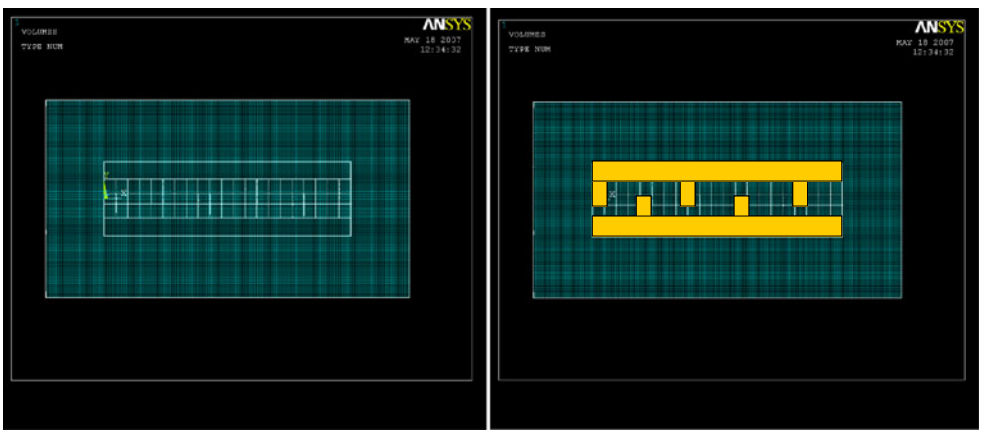

Fig. 4 3-D FEA model of the IDE beam

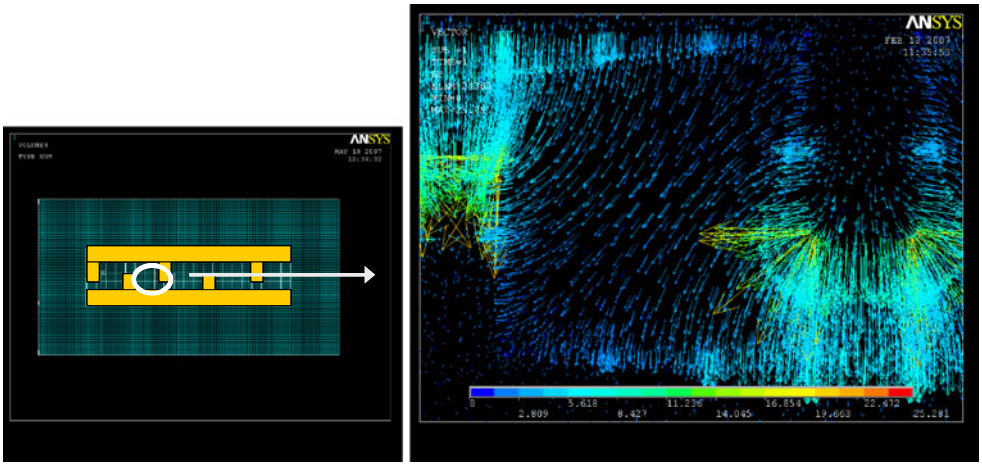

Fig. 5 Electric field between two electrodes for the IDE beam

It is important to point out that an assumption is made in this work that the piezoelectric material will be poled according to the electric field lines. In reality, however, this may not be the case due to hysteresis effects. For example, some areas may not be poled if the field is too low. Nonetheless, since this analysis is does take the simulated field lines into consideration, it should give a much better prediction of poling properties, particularly the reduction in poling associated with misdirected field lines, than the simplified ideal poling assumptions used in the past.

In addition to the curved electric field lines between electrodes, non 3-direction electric field also exists under the electrodes. This is shown in Fig. 6. Non 3-direction electric field implies that the piezoelectric layer is not completely poled in a single direction. Therefore, in the region underneath the electrodes, stress in the 3-direction cannot be completely coupled with the d_{33} constant of the material.

No method has been developed that investigates the exact loss associated with IDE poling in these two scenarios, between and under the electrodes. Eqs. (8) and (9) use a $\%d_{33}$ factor that represents the amount of poling between each electrode that is actually in the assumed 3-direction. In order to characterize $\%d_{33}$ FEA is utilized.

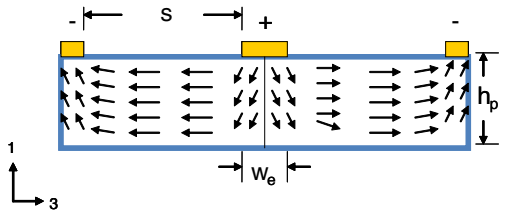

Fig. 6 Illustration of the non-uniform electric field that exists underneath the electrodes during poling

3.2 Interdigitated electrode FEA optimization

In order to characterize the non-uniform poling orientation developed from the high electric field applied during poling, the results of the FEA analysis were analyzed. The FEA model can be used to optimize the IDE design. Similar work was also done in Bowen et al. [36]. However, Bowen considered a PZT-fiber composite with, more importantly, IDEs on both the top and bottom sides of the sample. The IDE considered here has only one IDE pattern which is on top of the beam. Becket and Kreher [37] presented analysis of the IDE design for a piezoelectric bulk film and a composite with piezoelectric fibers as the piezoelectric active component. To date no resource has been published that examines a MEMS scale unimorph IDE poling electric field. The results found here are higher than what was found in Bowen because of different IDE pattern and poling condition.

A 2-D ANSYS™ model was made consisting of two electrodes on top of a PZT layer. The PZT layer was mounted on top of a substrate layer. Figure 7 illustrates the ANSYS 2-D model and its corresponding dimensions. Here the electrode width w_e is divided by two electrodes, $w_e' = w_e/2$, because when a structure has multiple fingers in the IDE pattern half the electrode is associated with one poling direction and the other half electrode is associated with the other poling direction.

Plane 230 elements were used to model the electric field produced during poling. Table 1 lists the electric properties used in the simulation. The values are scaled down to μMKS units.

Referring to Fig. 7 the simulation was conducted as follows:

- The spacing, s between the electrodes was varied from 1.0-40.0 μm.

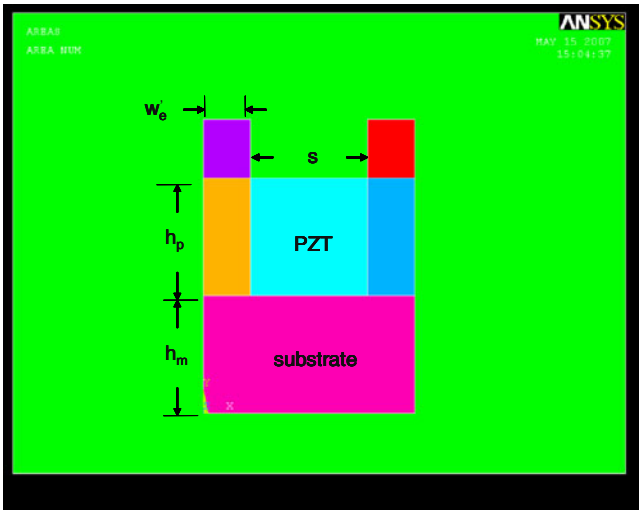

Fig. 7 2-D ANSYS model with variable dimensions

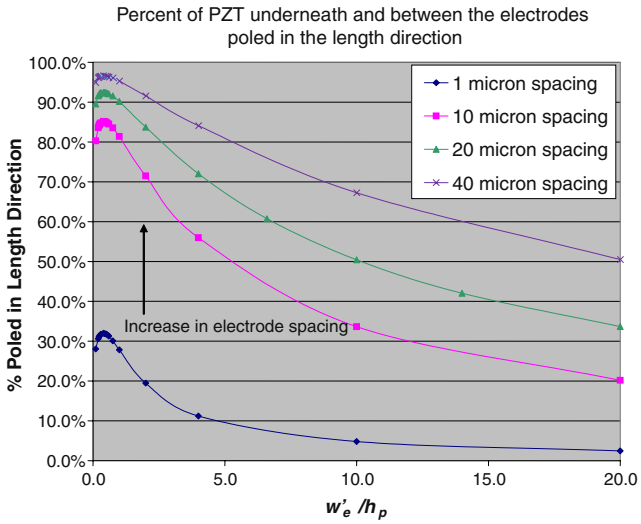

Fig. 8 ANSYS IDE spacing optimization for various electrode width to piezoelectric layer thickness ratios

- For each spacing value the ratio, w'_e/h_p was varied from 0.1–20.0.
- The poling voltage was dependent on the spacing, s and was equal to $V_{poling}=4s$.
- After each simulation the 3-direction electric field was integrated inside the PZT area that contains both the area between and under the electrodes.
- The integration value was averaged by dividing by the total PZT area, $(w_e+s)h_p$.
- The average electric field in the length direction was then divided by the input electric field value to get a value for the percent of poled PZT in the length direction.

Figure 8 shows the results from the ANSYS optimization. The plot illustrates the percent of PZT poled ($(\%\ poled)_{IDEoptimization}$) in the beam length direction for both increasing electrode width to PZT layer thickness ratio and electrode spacing.

It was concluded that after a w'_e/h_p ratio of 2 for any spacing the percent poled in the length direction, the assumed 3-direction, dramatically reduced.

For each spacing the w'_e/h_p ratio was optimal at about $w'_e/h_p = 0.4$. Figure 8 considers the electrode width divided by two. When $w'_e/h_p = 0.4$ the length direction electric field density was nearly maximum for every spacing value. A maximum percent poled value of 100% considers the PZT layer fully poled in the length direction. As spacing increases the percent of PZT poled in the length direction will approach 100%. This is purely because the spacing is becoming much larger than the electrode width, so the portion of angled electric field lines is relatively smaller. There is an optimal ratio (with peak percent poling value) because for small ratios (narrow electrode and/or thick piezoelectric layer), the electric field lines cannot penetrate all the way through the thickness of the PZT layer, while for large ratios (wide electrodes or thin piezoelectric layer) much of the poling is vertical under the electrode. At the optimal electrode width to piezoelectric layer height, the electric field can penetrate to the bottom of the PZT layer with the minimum electrode width necessary. Doubling the optimal w'_e/h_p ratio of 0.4 and accounting for back-to-back IDEs (that is, h_p in this paper is effectively 1/2 the h_p value used in the Bowen work) would give a comparative w_e/h_p ratio of 1.6. This differs from the optimal electrode width to substrate thickness ratio, 0.5, presented in Bowen et al. [36]. The larger ratio value is expected since the current analysis only considers a single IDE pattern in comparison to Bowen's dual IDE pattern (being on both the bottom and top of the piezoelectric material). It is also noted that Bowen's analysis did not consider poling, but only driving of an already poled system was considered. Adding an IDE pattern on the bottom of the piezoelectric layer allows for the electric field from each IDE to only have to penetrate half way through the thickness, thus allowing a smaller electrode width to substrate thickness ratio.

Table 1 Electrical values used for IDE optimization

Material	Relative permittivity	Resistivity [Ohm/μm]
Air	1.0005	3.00E+07
PZT	x–900	
	y–900	1.00E+00
	z–1100	
Electrode	0	1.00E-14
Substrate	4	1.00E+07

3.3 Planar interdigitated electrode loss

Figure 9 shows a top view of a typical IDE layout. In order to connect all the electrodes, electrode strips have to run down each side of the PZT's surface. These electrode strips produce an inadvertent electric field in the width direction of the beam.

The electric field during poling is now defined by the following equation

$$\underline{E} = E_2\underline{e_2} + E_3\underline{e_3} \tag{11}$$

where

$$E_2 = \frac{V_p}{W} \tag{12}$$

$$E_3 = \frac{V_p}{s} \tag{13}$$

$$\theta = \arctan\left(\frac{s}{W}\right) \tag{14}$$

As W decreases the electric field becomes stronger in the 2-direction and θ increases. The electro-mechanical coupling from a 3-direction stress becomes correspondingly smaller. Figure 10 is a plot that illustrates how the percentage of poling ($(\%poled)_{planar}$) is dependent on the beam width to electrode spacing, W/s, ratio.

Figure 10 illustrates that if the beam width to electrode spacing is large enough, the % of poling will be almost 100%. This is because the electric field in the width direction of the beam becomes weak relative to the electric field in the length direction.

After doing the FEA optimization and planar electrode loss analyses the following was gained:

- The performance of PZT is highly dependent upon the electrode layout.
- Large spacing and small w_e/h_p ratios allow the majority of the PZT to be poled.
- The optimal output (best performance) of the IDE beam has a w_e/h_p ratio was 0.8.
- Making the beam width large with respect to the spacing increases the amount of material poled in the 3-direction.

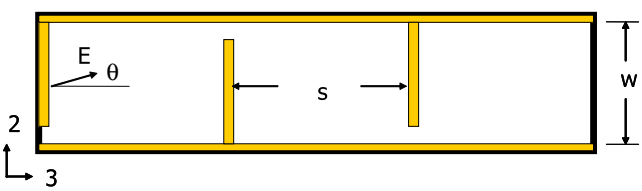

Fig. 9 Top view of IDE layout

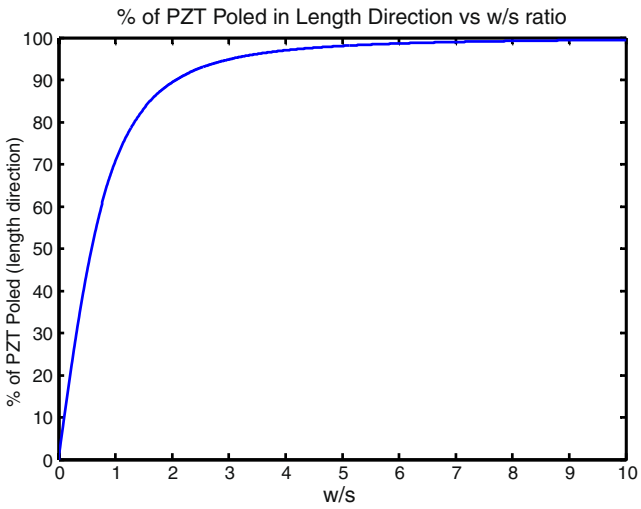

Fig. 10 % of poling plot under a constant electric field for the IDE layout in Fig. 9

There is a design tradeoff between both the poling analysis and optimal ratio discovered versus the beam's width loss. In order to pole the majority of material underneath the electrode the spacing should be large (large enough so the PZT can still be poled without arching) while keeping the w_e/h_p ratio equal to 0.8. But increasing the electrode spacing means the resulting beam's width has to be increased as depicted in Fig. 10. So depending on the length of the beam, the beam design could be more like a plate.

For MEMS IDE beams it is important to consider the optimal w_e/h_p ratio when choosing the fabrication processes. For example, considering a standard photolithography process that has feature size limitations of 1 to 3 μm (which would imply the lower limit for electrode width) obtaining the optimal ratio of electrode width to piezoelectric layer spacing would require a PZT layer thickness of up to 3.75 μm. A 3.75 μm thickness is very large for a sol-gel process and is hard to produce crack/hillock-free. Therefore, particular attention must be given to the processing steps to be able to create small electrode feature sizes. Secondary to the w_e/h_p ratio, other important design parameters for MEMS IDE devices are the electrode spacing and the width of the beam.

The above three findings help address the issue of when is it advantageous to use IDE structure in comparison to a d_{31} unimorph structure. Since d_{33} is typically more than twice as large as d_{31}, the IDE beam design becomes the preferred choice when the percent of material poled in 3-direction is approximately 50% (in which case, the IDE design is more effective than the d_{31} beam). In order to obtain the total value of the poled PZT, the percent poled value from the IDE optimization must be multiplied by the

percent poled value in planar analysis. This relationship is shown as

$$\%\, d_{33} = (\%poled)_{IDEoptimization} \times (\%poled)_{planar} > 50\% \quad (15)$$

If Eq. 15 is not met then one should design a d_{31} unimorph.

In order to help meet Eq. 15 the IDE d_{33} unimorph should be designed to have the largest spacing and the beam's width allowable. Both of these parameters will increase the percent poled factors. After determining the amount of PZT that can be poled in the length direction, one can make a better design decision on whether to use a d_{33} unimorph or a d_{31} unimorph.

4 Conclusion

Two types of MEMS cantilever beams as energy harvesters, d_{31} unimorph and d_{33} unimorph, were investigated for better design in terms of energy generating performance both mathematically and by FEA. The capacitance ratio and the generated charge ratio of the d_{33} beam to d_{31} beam were first developed in order to compare the performance of each design. The d_{33} unimorph equations were derived using a percent poling factor. The percent poling factor arises from the non-uniform electric field during piezoelectric layer poling. The percent poling factor was then investigated. ANSYS™ was used to simulate various electrode width to PZT layer thickness ratios (w_e/h_p) for four different electrode spacing values. Additionally, a percent output in the length direction was determined for each spacing w_e/h_p ratio. For every electrode spacing value, an optimal w_e/h_p was found to be consistently 0.8. As spacing increased the percent output in the length direction also increased.

The work presented will assist in the design of MEMS or macro scale piezoelectric devices. Choosing the proper intedigitated electrode layout and beam dimensions can nearly double the performance of a d_{33} unimorph device. Thus, designing a proper d_{33} unimorph device will increase energy harvesting performance. By following the design guidelines presented here, it is expected that even better performance can be obtained.

References

1. R. Sood, Y.B. Jeon, J.H. Jeong, S.G. Kim, *Piezoelectric Micro Power Generators for Energy Harvesting* (Technical Digest of the Solid-State Sensor and Actuator Workshop, Hilton Head USA, 2004)
2. Y.B. Jeon, R. Sood, J.H. Jeong, S.G. Kim, MEMS power generator with transverse mode thin film PZT. Sens Actuators A **122**, 16–22 (2005)
3. W.J. Choi, Y. Jeon, R. Sood, S.G. Kim, Energy harvesting MEMS device based on thin film piezoelectric cantilevers. J Electroceram **17**, 543–548 (2006)
4. D. Shen, J.H. Park, J. Vjitsaria, S.Y. Choe, H.C. Wikle, D.J. Kim, The design, fabrication and evaluation of a MEMS PZT cantilever with an integrated Si proof mass for vibration energy harvesting. J Micromech Microeng **18**, 055017 (2008). 7 pp
5. B.S. Lee, S.C. Lin, W.J. Wu, X.Y. Wang, P.Z. Chang, C.K. Lee, Piezoelectric MEMS generators fabricated with an aerosol deposition PZT thin film. J Micromech Microeng **19**, 065014 (2009). 8 pp
6. E.K. Reilly, P.K. Wright, Modeling, fabrication and stress compensation of an epitaxial thin film piezoelectric microscale energy scavenging device. J Micromech Microeng **19**, 095014 (2009). 11 pp
7. Y.K. Hong, K.S. Moon, M. Levy, Single-crystal film piezoelectric sensors, actuators, and energy harvesters with interdigitated electrodes. Ferroelectric **342**, 1–13 (2006)
8. S. John, J. Sirohi, G. Wang, "Comparison between PMN and PZT as a driving element in a compact hybrid actuator," in *Proc. of ISSS*, Vol. ISSS-2005/SA-15 (2005).
9. D.L. DeVoe, Piezoelectric thin film micromechanical beam resonators. Sens Actuators A **88**, 263–272 (2001)
10. L. Li, P. Kumar, L. Calhoun, D.L. DeVoe, Piezoelectric Al0.3 Ga0.7As longitudinal mode beam resonators. J MEMS **15**, 465–470 (2006)
11. G. Piazza, P.J. Stephanou, A.P. Pisano, One and two port piezoelectric higher order contour-mode MEMS resonators for mechanical signal processing. Solid State Electron **51**, 1596–1608 (2007)
12. C.L. Dai, C.H. Kuo, M.C. Chiang, Microelectromechanical resonator manufacturing using CMOS-MEMS technique. Microelectron J **38**(6–7), 672–677 (2007)
13. R.M.C. Mestrom, R.H.B. Fey, J.T.M. van Beek, K.L. Phan, H. Nijmeijer, Modelling the dynamics of a MEMS resonator: Simulations and experiments. Sens Actuators A **142**, 306–315 (2008)
14. J.L. Lopez, J. Verd, J. Teva, G. Murillo, J. Giner, F. Torres, A. Uranga, G. Abadel, N. Barniol, Integration of RF-MEMS resonators on submicrometric commercial CMOS technologies. J Micromech Microeng **19**, 015002 (2009). 10 pp
15. W. Pan, P. Soussan, B. Nauwelaers, A.C. Tilmans, A surface micromachined electrostatically tunable film bulk acoustic resonator. Sens Actuators A **126**, 436–446 (2006)
16. H. Chandrahalim, S. A. Bhave, E. P. Quevy, R. T. Howe, "Aqueous transduction of poly-SiGe disk resonators," *14th Int. Conf. Solid-State Sensors, Actuators and Microsystems*, 313–316 (2007).
17. H. Chandrahalim and S. A. Bhave, "Digitally-tunable MEMS filter using mechanically-coupled resonator array," *IEEE conf. on MEMS*, 1020-1023 (2008)
18. H. Chandrahalim, S.A. Bhave, R. Polcawich, J. Pulskamp, D. Judy, R. Kaul, M. Dubey, Perfromance comparison of Pb($Zr_{0.52}Ti_{0.48}$)O_3-only and Pb($Zr_{0.52}Ti_{0.48}$)O_3-on-silicon resonators. Appl Phys Lett **93**, 233504 (2008)
19. T. Kawakubo, T. Nagano, K. Abe, M. Nishigaki, T. Ono, "Piezoelectric MEMS element and tunable filter equipped with the piezoelectric MEMS element," *US Patent Number* 7,471,031 B2, (2008).
20. G. K. Ho, F. Ayazi, S. Pourkamali, K. Sundaresan, "Highly tunable low-impedance capacitive micromechanical resonators, oscillators, and process relating thereto," *US Patent Number* 7,511,870 B2, (2009).
21. I. Zine-El-Abidine, P. Yang, A tunable mechanical resonator. J Micromech Microeng **19**, 125004 (2009)

22. F. Nabki, K. Allidina, F. Ahmad, P.V. Cicek, M.N. El-Gamal, A Highly Integrated 1.8 GHz Frequency Synthesizer Based on a MEMS Resonator. IEEE J Solid State Circ **44**(8), 2154–2168 (2009)
23. A.A. Frederick, *Analysis and Fabrication of MEMS Tunable Piezoelectric Resonators* (University of Pittsburgh, Pittsburgh, MS Thesis, 2006)
24. R. Knight, *The Analysis and Testing of MEMS and Macro Scale Piezoelectric Devices* (University of Pittsburgh, Pittsburgh, M.S. Thesis, 2007)
25. W.W. Clark, "Vibration Control with State-Switched Piezoelectric Materials," *J. of Intelligent Material Systems and Structures*, **11** (2000).
26. C. L. Davis, G. Lesieutre, J. Dosch, "A tunable electrically shunted piezoceramic vibration absorber," *Proc. SPIE*, **2045** (2003).
27. G. Lesieutre, G. Ottman, H. Hofmann, Damping as a result of piezoelectric energy harvesting. J Sound Vib **269**, 991–1001 (2004)
28. M. Muriuki, *An Investigation into the Design and Control of Tunable Piezoelectric Resonators* (University of Pittsburgh, Pittsburgh, Ph.D Dissertation, 2004)
29. W. Wu, Y. Chen, B. Lee, J. He, Y. Peng, "Tunable resonant frequency power harvesting devices," *Proc. of SPIE*, Smart Structures and Materials, Damping and Isolation, **6169** (2006).
30. S. Kim, *Low Power Energy Harvesting with Piezoelectric Generator* (University of Pittsburgh, Pittsburgh, Ph.D Dissertation, 2002)
31. C. Mo, S. Kim, W. W. Clark, "Analy**sis** of Power Generating Performance for Unimorph Cantilever Piezoelectric Beams with the Interdigitated Electrode," in *Proc. of IDETC/CIE,* (ASME, San Diego USA, 2005).
32. C. Mo, S. Kim, W.W. Clark, Theoretical analysis of energy harvesting performance for unimorph piezoelectric benders with interdigitated electrodes. Smart Struct Mater **18**, 5 (2009)
33. H. A. Sodano, J. Lloyd, D. J. Inman, "An experimental comparison between several active composite actuators for power generation," in *Proc. of SPIE on Smart Structures and Materials*, (SPIE, San Diego USA, 2004), vol. 5390.
34. H.A. Sodano, D.J. Inman, G. Park, Comparison of piezoelectric energy harvesting devices for recharging batteries. J Intell Mater Syst Struct **16**, 10 (2005)
35. ANSYS™, *Coupled-Field Analysis Guide*, Release 10.0 Documentation for ANSYS.
36. C.R. Bowen, L.J. Nelson, R. Stevens, Optimisation of interdigitated electrode for piezoelectric actuators and active fibre composites. J Electroceram **16**, 263–269 (2006)
37. W. Becket, W. Kreher, Modelling piezoelectric modules with interdigitated electrode structures. Comput Mater Sci **26**, 36–45 (2003)